RIS-Assisted Coverage Enhancement in Millimeter-Wave Cellular Networks

MAHYAR NEMATI[ID], **(Member, IEEE), JIHONG PARK**[ID]**, (Member, IEEE), AND JINHO CHOI**[ID]**, (Senior Member, IEEE)**
School of Information and Technology, Deakin University, Geelong, VIC 3220, Australia

Corresponding author: Mahyar Nemati (nematim@deakin.edu.au)

ABSTRACT The use of millimeter-wave (mmWave) bandwidth is one key enabler to achieve the high data rates in the fifth-generation (5G) cellular systems. However, mmWave signals suffer from significant path loss due to high directivity and sensitivity to blockages, limiting its adoption within small-scale deployments. To enhance the coverage of mmWave communication in 5G and beyond, it is promising to deploy a large number of reconfigurable intelligent surfaces (RISs) that passively reflect mmWave signals towards desired directions. With this motivation, in this work, we study the coverage of an RIS-assisted large-scale mmWave cellular network using stochastic geometry, and derive the peak reflection power expression of an RIS and the downlink signal-to-interference ratio (SIR) coverage expression in closed forms. These analytic results clarify the effectiveness of deploying RISs in the mmWave SIR coverage enhancement, while unveiling the major role of the density ratio between active base stations (BSs) and passive RISs. Furthermore, the results show that deploying passive reflectors are as effective as equipping BSs with more active antennas in the mmWave coverage enhancement. Simulation results confirm the tightness of the closed-form expressions, corroborating our major findings based on the derived expressions.

INDEX TERMS Millimeter-wave (mmWave), reconfigurable intelligent surface (RIS), coverage, signal-to-interference ratio (SIR), stochastic geometry.

I. INTRODUCTION

Millimeter-wave (mmWave) cellular networks are widely studied for the emerging fifth generation (5G) of mobile communication networks and beyond. The Asia-Pacific region is supposed to give rise to the greatest share of the total contribution of mmWave communications to the gross domestic product (GDP), i.e., $212 billion, over the period 2020 to 2034 [1]; with a compound annual growth rate of 31% in the volume of mobile data traffic [2]. These significant growths imply that within the next decades, mmWave cellular networks will have significantly drawn attention to deliver much higher data-rate and capacity compared to current levels due to the availability of wider bandwidths [3]–[5].

As a primary distinctive technical feature, the mmWave band suffers from a higher path loss than sub-6 GHz band. As a result, the mmWave communication range is limited. Nevertheless, when the frequency increases, the

The associate editor coordinating the review of this manuscript and approving it for publication was Danping He[ID].

wavelength decreases which results in antenna aperture reduction. Thanks to a short wavelength (1 − 10 mm), it is feasible to pack multiple antenna elements into limited space at mmWave transceivers [6]. With large antenna arrays, e.g., multiple-input multiple-output (MIMO), mmWave cellular systems can execute beamforming to provide an array gain that compensates the frequency dependent path loss and overcomes additional noise power [6]–[8]. However, the mmWave communication range is still restricted due to the mmWave propagation characteristics, e.g., scattering, diffraction, and penetration loss [7], [8]. For instance, communications in mmWave frequencies highly suffer from penetration losses resulting in a blockage effect which mainly affects the line-of-sight (LoS) path and non-LoS (NLoS) path loss characteristics [6].

Wireless transmission through multiple identified paths utilizing active MIMO relaying has been proposed as a potential solution that can reduce the blockage effect and increase the diversity [9], [10]. However, in [11]–[13], it is shown that full-duplex MIMO relaying has a number of drawbacks such

as signal processing complexity, noise enhancement, power consumption and self-interference cancellations at the relay stations along with their high implementation costs. To this end, it would be desirable to control the propagation environment in those frequencies with simple low-cost full-duplex passive reflectors like what has been recently proposed as in **reconfigurable intelligent surfaces (RISs)** [12] to mitigate the aforementioned drawbacks.

An RIS is a software-defined metasurface containing a large number of passive reflectors and has given rise to the emerging "smart radio environments" concept [12]. The recent advent of RISs in wireless communications enables network operators to control the reflection characteristics of the radio waves in an energy efficient-way [14]. The passive reflectors in an RIS are intelligently controlled by a main integrated circuit (IC) to adjust phase-shift of an impinging signal. Note that the RIS design operates like a nearly-passive surface rather than a fully passive model, since the surface itself does not generate new RF signals, but it can be adaptively configured by a low power IC in order to beamform and to focus the impinging RF signals towards specified direction and locations, respectively [15]. In other words, RIS can turn the wireless environment, which is highly probabilistic, into a controllable and partially deterministic phenomenon [11], [16]. It is also noteworthy that RIS mechanism does not include any mechanical action or tilt like what has been widely used in micro-electro-mechanical systems (MEMS) [17], [18]. Instead, these cheap and low-complex RIS-elements are made by electromagnetic (EM) material that are electronically controlled with a main IC and have unique wireless communication capabilities including conventional reflect-arrays, liquid crystal surfaces, and software-defined meta-surfaces [11], [12], [17]–[22]. Furthermore, the channel estimation in RIS-assisted systems was investigated in [23]–[27].

In the literature, there is a significant effort to model mmWave cellular networks under different circumstances using stochastic geometry [6], [28]–[30]. As early works, general stochastic geometry frameworks of mmWave cellular network were proposed in [6], [28] to model the static objects and corresponding blockage probability using the concept of random shape theory. Moreover, the impact of relay on a multi-hop medium access control protocol for 60 GHz frequency was investigated in [29] when the LoS path is blocked. In [10], [30], comprehensive coverage performance analysis of relay-assisted mmWave cellular networks were investigated. However, the aforementioned studies did not consider the spatial randomness of RISs deployments. In addition, the study of impact on RIS deployment in mmWave cellular networks is limited. In [17], [31]–[33], general comprehensive overviews characterizing the performance of RIS-assisted communications affecting the propagation environments were provided. Moreover, in [34]–[36], the impact of RIS deployments for non-orthogonal multiple access (NOMA) networks were assessed. In [37], authors investigated the RIS-aided multi-cell NOMA networks using

a stochastic geometry model. An analytical framework for evaluating the ergodic capacity (EC) of the RIS-assisted systems was presented in [38]. In [39], the effect of large-scale deployment of RISs on the performance of cellular networks was studied by modeling the blockages using the line Boolean model. In [40], an RIS-assisted MIMO framework was proposed to randomly serve users by jointly passive beamforming weight at the RISs and detection weight vectors at the users. In [41], an analytical probability framework of successful reflection of RIS for a given transmission was provided using point processes, stochastic geometry, and random spatial processes. In [42], authors proposed a distributed RIS-empowered communication network architecture, where multiple source destination pairs communicate through multiple distributed RISs. In [43], an optimal linear precoder along with an RIS deployment in a single cell for multiple users is used to improve the coverage performance of the communications. In [44], a characterization of the spatial throughput for a single-cell multiuser system assisted by multiple RISs that are randomly deployed in the cell was provided. It showed that the RIS-assisted model outperforms the full-duplex relay-aided counterpart system in terms of spatial throughput when the number of RISs exceeds a certain value. Most recently, an investigation on [45] discussed the potential use-cases of RISs in future wireless systems using a novel channel modeling methodology as well as a new software tool for RIS-empowered mmWave networks.

In this paper, we aim at studying a general tractable framework for the coverage performance of the RIS-assisted mmWave cellular networks with a major focus on RIS and BS densities. We use stochastic geometry as a powerful tool to study the average signal-to-interference-ratio (SIR) behavior over many randomly distributed BSs, RISs, and users in a 2-dimensional (2D) space. In our proposed model, BSs are equipped with a steerable antenna array and are able to send two beams towards a user equipment (UE). One beam is transmitted directly towards the UE, i.e., referred to as path **A**; and the other beam is sent towards the RIS and then reflected to the UE, i.e., referred to as path **B**. The main contributions of this paper are listed as follows.

- We propose a general tractable RIS-assisted approach for SIR coverage performance in mmWave cellular networks for the first time where the message is sent by the BS towards the UE through two different paths. We use a diversity technique in which the system profits from the maximum received SIR at the UE through either path **A** or path **B**.
- Since the reflected power of passive RIS-reflectors is largely affected by the distance between the active BS and the RIS due to large-scale fading, we provide the probability distribution function (PDF) of this distance as an important quantity and discuss its dependency on the RIS and BS densities.
- Discrete time delay values corresponding to quantized phase-shifts at each RIS-reflector is elaborated for passive beamforming at the RIS towards the UE.

In addition, the peak reflection power at the RIS is assessed. It is shown that the average peak reflection power at the RIS decreases when the active BS density decreases. However, the reflected power reduction can be compensated by employing RISs of a large number of passive reflectors.

- A closed-form approximation, referred to as **Approximation-I**, along with a lower bound approximation, referred to as **Approximation-II**, is derived for the SIR coverage probability of the signal received by the UE from path **B**, i.e., RIS-assisted path.

- Finally, we show that the RIS-assisted model provides a great deal of flexibility to obtain a desired SIR gain. Furthermore, we show that in large BS densities when the active BS density decreases, the co-channel interference caused by active interferer BSs decreases faster than the reflected power from the RIS. As a result, in large BS densities, the decrease of active BS density improves the SIR coverage probability in our RIS-assisted model.

The rest of the paper is organized as follows. In Section II, we present the system model of a baseline and RIS-assisted mmWave cellular networks. Then, the principles of RIS-assisted model are discussed in Section III. Subsequently, the SIR coverage analysis of the RIS-assisted model is provided in Section IV. A comprehensive discussion on both of the baseline and RIS-assisted models is given in Section V. Simulation results and comparisons are presented in Section VI. Finally, Section VII concludes the paper.

II. SYSTEM MODEL

In this section, we first present a baseline downlink mmWave cellular network, followed by introducing the RIS-assisted downlink mmWave network. The baseline network model follows the standard frameworks for stochastic geometric mmWave system analysis [46], [47], but for the reader's convenience, we briefly describe the basics.

We provide a set of common suppositions used for both baseline and RIS-assisted models as follows. In a blockage-free mmWave network, BSs are randomly located in a 2D space according to a homogeneous Poisson point process (PPP), denoted by Φ_{BS}, with an intensity of λ_{BS}. Furthermore, the UEs are distributed independently in the area, and each UE communicates with the nearest BS to enjoy the least mean propagation loss. The probability density function (PDF) of the distance between the UE and the nearest BS, denoted by r_0, is obtained from the void probability in Poisson process of $\mathbb{R}^2$ as follows [48]:

$$f_{r_0}(r_0) = 2\pi \lambda_{BS} r_0 e^{-\lambda_{BS}\pi r_0^2}. \tag{1}$$

It is noteworthy that so far, we consider a blockage-free scenario. In other words, the blockage effect is not considered in this study to simplify the analysis without loss of generality since it does not affect the conclusions of this study.

Specifically, objects that act as blockages for the communication links, e.g., buildings and trees, can be equipped with RISs to provide indirect LoS links between the UE and the BS and consequently the reflections enable the network to overcome blockages as observed in [39]. Thus, we envisage that RISs will further enhance the network coverage under blockages, and investigating this is deferred to our future work.

We assume that all the BSs are equipped with N isotropic active elements for beamforming towards the targets while the UEs are equipped with single omnidirectional antenna. Furthermore, the recent works in [47], [49] have shown that the empirical distribution of small-scale fading effects of the channel and the beamforming gain of the antenna array can be tightly approximated by using *exponential* distribution. Thus, in order to maximize the mathematical tractability of our analysis, we consider the following assumption for the small-scale fading channel gain.

Assumption 1 (Small-Scale Channel Gain): The small-scale fading gain is assumed to follow an exponential distribution with mean of $1/\mu$. In the past, this assumption was common in stochastic geometric coverage analysis for mathematical tractability [6], [47], [49]–[53]. Recent works [47], [49] revisited this exponential fading assumption, and rediscovered its feasibility even under realistic large-scale mmWave systems, by simply tuning μ according to the mean channel characteristics and antenna patterns. To be more specific, authors in [47] explained that the channel gain in mmWave systems is affected not only by the channel randomness but also by the antenna array directions. Consequently, in [47, Remark 5], simplified channel and radiation approximations are provided showing that the channel gain at the typical UE independently follow an exponential distribution, i.e., for ISO antenna model, $\mu \approx \frac{1}{n_t n_r}$ where n_t and n_r are the number of antenna elements at the transmitter and receiver sides, respectively.

A. BASELINE mmWave CELLULAR NETWORK

Figure 1 depicts the baseline mmWave cellular network where each BS creates one beam to send the downlink signal towards the desired UE. The transmit signal power at the active BSs is assumed to be constant and is denoted by P_s. Compared to the sub-6 GHz cellular networks in [46], in the mmWave cellular networks, beamforming is used to converge the signal power in a specific direction towards a desired UE due to the mmWave propagation characteristics [54]. The existing coverage analysis in [46] evaluated the conventional cellular networks for sub-6 GHz frequency bands. We exploit their analysis and modify it to introduce our baseline mmWave cellular network while taking beamforming into account. In general, as shown in Figure 1, there are two types of signal power sources. One type is the desired signal power received by the UE from the associated BS as the desired source, and the other type is the interference signal power received by the UE from the interferer BSs. Based on the uniform planar square array (UPA) in 2D space [54],
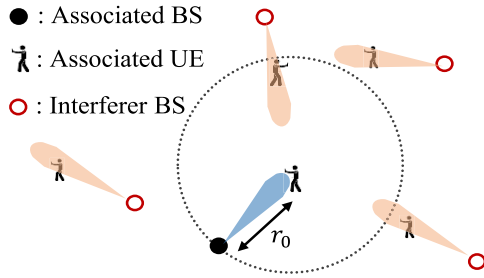
FIGURE 1. Depiction of the baseline mmWave cellular network.

FIGURE 2. Depiction of the RIS-assisted mmWave cellular network.

the active BSs with N isotropic elements are able to create single beam with beamwidth:

$$\psi_o = \frac{2\pi}{\sqrt{N}}. \tag{2}$$

Let each interferer BS transmit with its main-lobe pointed at a random direction. Nevertheless, as an additional gain, it also reduces co-channel interference because the signal from any NLOS interferer is highly attenuated [55]. Intuitively, it affects the density of interferer BSs as a modified homogeneous PPP, denoted by Φ_I, with an intensity of λ_I as follows:

$$\lambda_I = \frac{\lambda_{BS}}{\sqrt{N}}. \tag{3}$$

In other words, only a subset of interferer BSs in which their beamforming direction covers the desired UE are considered to be effective interferer BSs for the UE.

Let Γ_o denote the SIR at an independent UE in the baseline mmWave cellular network. In this paper, we omit the noise power in SINR and evaluate the SIR-based performance for simplicity. Consequently, the SIR can be obtained as

$$\Gamma_o = \frac{P_s g_0 r_0^{-\alpha}}{\sum\limits_{\substack{BS_i \in \Phi_I, \\ i \neq 0}} P_s g_i r_i^{-\alpha}} = \frac{g_0 r_0^{-\alpha}}{\sum\limits_{\substack{BS_i \in \Phi_I, \\ i \neq 0}} g_i r_i^{-\alpha}}, \tag{4}$$

where g_i and r_i are small-scale channel gain and the distance between the ith BS, denoted by BS_i, and the UE, respectively. Here, $i = 0$ indicates the nearest BS which is the associated BS and α is the path-loss exponent of large-scale fading. From *Assumption 1*, we have $g_i \sim \exp(\mu)$ for all i.

For the SIR coverage probability which is the probability that the received SIR is larger than a threshold, let T denote the threshold. Then, from (4) and similar to the analysis in [46], the SIR coverage probability is given by

$$\Pr\left[\Gamma_o > T\right] = \mathbb{E}\left\{\Pr\left(\frac{g_0 r_0^{-\alpha}}{\sum\limits_{BS_i \in \Phi_I} g_i r_i^{-\alpha}} > T\right)\right\}. \tag{5}$$

In other words, it is equivalent with the complementary cumulative distribution function (CCDF) of SIR. Eventually, after some analysis given in Appendix VII and similar to [46], we
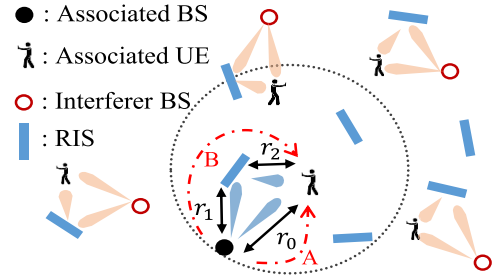
have

$$\Pr\left[\Gamma_o > T\right] = \frac{1}{1 + \frac{1}{\sqrt{N}} T^{\frac{2}{\alpha}} \int_{T^{-\frac{2}{\alpha}}}^{\infty} \frac{1}{1 + u^{\frac{\alpha}{2}}} du}. \tag{6}$$

It is noteworthy that the final coverage probability expression is independent of the BSs' transmit power and density. It only depends on the beamwidth of the beams (i.e., N), T, and α.

B. RIS-ASSISTED mmWave CELLULAR NETWORK

Suppose that there are buildings equipped with RISs in a mmWave cellular network which are distributed based on a homogeneous PPP, denoted by Φ_{RIS}, with an intensity of λ_{RIS}. Each RIS has two parts: 1) passive part containing M passive reflectors, and 2) a simple active part acting as a phase-shift controller. Figure 2 shows the associated BS and the UE in the coexistence of RISs and other interferer BSs. Suppose the nearest RIS to the UE is in distances of r_1 and r_2 from the associated BS and the UE, respectively. Then, the UE communicates with the nearest RIS along with the nearest associated BS when there is an RIS closer to the UE than the distance between the BS and the UE, i.e., $r_2 < r_0$. In other words, different from the baseline model, here when there is an RIS closer to the UE than the distance between the BS and the UE, i.e., $r_2 < r_0$, the associated BS divides its single beam into two similar beams. The first beam is transmitted directly towards the desired UE, and the second beam targets the nearest RIS to the UE as shown in Figure 2. It is noteworthy that since the location of BSs and RISs are fixed, BSs are aware of the surrounding RIS locations. Consequently, by receiving the UE response to the paging message broadcasted from the associated BS and identifying its location (assuming the BS capability of passive localization [56]), the BS can decide which RIS is closer to the UE to split the power between two beams. As a result, the beamwidth of each of these two beams changes, from (2) in the baseline model, into

$$\psi_s = \frac{2\sqrt{2}\pi}{\sqrt{N}}, \tag{7}$$

in 2D space and the transmit power of each beam at the active BSs becomes $\frac{P_s}{2}$. Nevertheless, this happens only when $r_2 < r_0$. The PDF of r_2 can be obtained from the void probability in Poisson process of $\mathbb{R}^2$ as

$$f_{r_2}(r_2) = 2\pi \lambda_{RIS} r_2 e^{-\lambda_{RIS} \pi r_2^2}. \tag{8}$$

(a) Baseline model.   (b) RIS-assisted model.
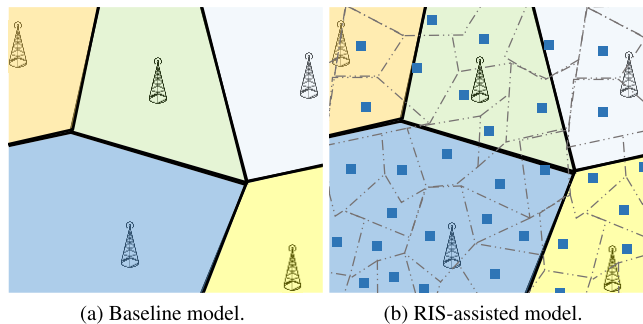
FIGURE 3. Comparison between the baseline and RIS-assisted models when $\lambda_{RIS} \gg \lambda_{BS}$. Squares indicate RISs. In RIS-assisted model, each RIS has its own coverage area since the UE communicates with the nearest RIS.

FIGURE 4. The idle RIS reflects the signals toward the empty spaces, e.g. Sky.

With the analysis given in Appendix VII, the probability of having an RIS within the distance between the associated BS and the UE becomes

$$f_{r_2}(r_2|r_2 < r_0) = 2\pi(\lambda_{RIS} + \lambda_{BS})r_2 e^{-\pi(\lambda_{RIS}+\lambda_{BS})r_2^2}. \quad (9)$$
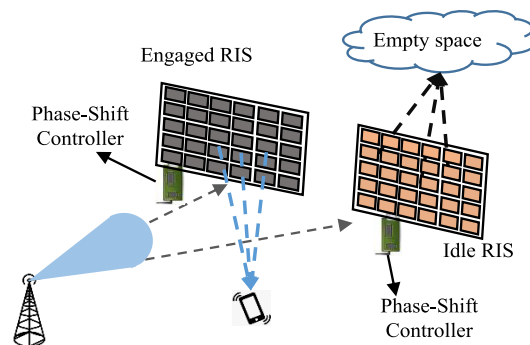
Throughout the paper, we consider $\lambda_{RIS} \gg \lambda_{BS}$, as shown in Figure 3. Since RISs are passive, they are easier and cheaper to be implemented than the active BSs. Therefore, it satisfies the given condition of $r_2 < r_0$ and the expression in (9) approximately becomes equivalent to (8), i.e.,

$$\lambda_{RIS} \gg \lambda_{BS} \rightarrow f_{r_2}(r_2|r_2 < r_0) \approx f_{r_2}(r_2). \quad (10)$$

Thus, in general, there are two different paths from the BS towards the UE as shown in Figure 2. One path which is directly from the BS to the UE, i.e., referred to as path **A**; and the other path which goes through the RIS and then reflected towards the UE, i.e., referred to as path **B**. Let assume each RIS serves one UE at a time.[1] The phase-shift controller at the RIS can adjust the phase-shifts and generate a new beam towards the UE (as described in section III-A). In fact, the RIS acts as a passive beam-former by adjusting the phase-shifts at the passive reflectors and converge a beam in a specific direction. Thus, we define two states for RISs with respect to their reflection directions as shown in Figure 4 since the passive elements are always on and reflect the impinging signals at all time, regardless of whether there is any UE associated with it or not [57].

- Engaged: The nearest RIS to the UE which is engaged for the communication assistant in path **B**.
- Idle: All other RISs which are not engaged in any communication are considered idle RISs. This is the default state when the phase-controller in an idle RIS adjusts the phase-shifts at the reflectors somehow to generate a beam towards an empty space, e.g., sky, to avoid

interference with the UEs. Intuitively, it is evident that the idle RISs do not contribute to an interference.

In a nutshell, the anatomy of the communication initiation is briefly explained as follows.

- The BS broadcasts the UE identification number as a paging message.
- Mobile receives the paging message and identifies itself along with its location to the BS and nearby RISs and a successful handshake between the BS and the UE takes place.[2]
- Subsequently, the BS which knows the location of the UE and fixed RISs around it, informs the UE and its nearest RIS which forward channel the UE has been assigned.
- The associated RIS becomes an engaged RIS and its phase-controller adjusts the phase-shifts at the reflectors.

Assumption 2: An engaged RIS is able to create a beam with highly narrow beamwidth toward the UE since it contains a large number of reflectors. Moreover, the reflection steering angle of each RIS is only limited to $[0, \pi]$. Thus, it may receive signal only from a half of the interferer BSs.[3] Intuitively, it significantly reduces the probability that the engaged RIS contributes to an effective interference. Therefore, throughout the paper, we neglect the interference that may be caused by engaged RIS reflections.[4]

In the following section, we explain the principles of the RIS-assisted mmWave cellular networks in more details.

III. PRINCIPLES OF RIS-ASSISTED mmWave CELLULAR NETWORK

In this section, first, we explain the phase-shift adjustment at each passive RIS-reflector and how passive beamforming is done by RISs. Second, a channel model for the RIS-assisted

---

[1]One RIS can serve multiple UEs assuming the size of the RIS is determined based on the density of UEs around it. Hence, in high density UE areas, a larger RIS is needed where a portion of its reflectors can be dedicated to each UE. However, this can be considered as another resource allocation problem which its further assessment is out of the scope of this paper. Therefore, without loss of generality, we assume that each RIS serves one UE at a time.

[2]It is noteworthy that angle of arrival of the UE's response can be simply obtained by both the BS and RIS with passive localization methods [56].

[3]Besides, since the RISs are passive and their reflected power significantly being affected by large-scale path-loss, they can only cause an interference for nearby UEs.

[4]Recently, authors in [57] showed that the interference marginally increases by RISs deployments. However, in order to maximize the mathematical tractability, we ignore this limited interference.
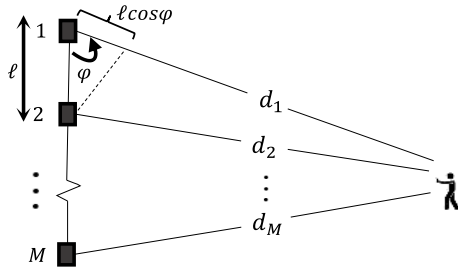
FIGURE 5. Depiction of *M*-passive-elements linear phased-array at the RIS.

path is discussed. Third, a distribution function for the distance between the associated BS and the engaged RIS is provided. Finally, the peak reflection power at the RIS is assessed.

A. PHASE-SHIFT ADJUSTMENT AT RIS AND PASSIVE BEAMFORMING

Seeing that the RIS includes M passive reflective elements, it does not generate any transmit power by its own. The phase controller of the RIS determines the phase-shift for each reflected signal to create a new beam towards the UE. Let assume that it is only able to adjust discrete phase-shifts for the impinging signal at each passive reflector due to the implementation constraints. In particular, in order to show the effect of M passive reflectors of the RIS on the transmit power, and also the phase-shift at each reflector, let simplify the generic 2D phased-array by applying it into a 1D linear phased-array [58] as shown in Figure 5; where the distance between the passive reflectors is denoted by ℓ and distance of the mth passive reflector to the UE is denoted by d_m, where $m = 1, \cdots, M$. Let $s(t + \delta_m)$ denote the message impinging the mth passive reflector at the RIS where δ_m stands for the phase difference of the impinging message at the mth reflector. Then, the reflected signal towards the UE which is a superposition due to M passive reflectors is given by

$$
\begin{aligned}
x(t) &= \sum_{m=1}^{M} s\left(t + \delta_m - \frac{d_m}{c} - \tau_m\right) \\
&= \sum_{m=1}^{M} s\left(t + \delta_m - \frac{d_1}{c} + \frac{m\ell \cos\varphi}{c} - \tau_m\right), \quad (11)
\end{aligned}
$$

where c, φ and τ_m correspond to the wave-speed, angle of the 1th element reflection toward the UE (as shown in Figure 5) and time delay of the mth reflector. Here, the time delay, τ_m, is associated with the phase-shift adjustment at the mth reflector. In other words, τ_m is given by

$$
\tau_m = \frac{m\ell \cos\varphi}{c} + \delta_m. \quad (12)
$$

Therefore, the reflected signal in (11) becomes

$$
x(t) = \sum_{m=1}^{M} s\left(t - \frac{d_1}{c}\right) = M s\left(t - \frac{d_1}{c}\right). \quad (13)
$$

Consequently, the RIS executes a new passive beamforming towards the UE, i.e., in an angle of φ, where the maximum power of the beam, i.e., peak effective radiated power, scales up by M^2. In addition, in order to put the phase-shift adjustment at each reflector into action, we may need to consider implementation constraints since $\frac{m\ell \cos\varphi}{c} + \delta_m$ might be continues values. However, we consider discrete values for τ_m that there will be a minimum phase-shift adjustment. We quantize the continues phase-shift amplitudes by discretizing them into the implementable values.

B. BS-RIS AND RIS-UE CHANNEL MODELS

In this subsection, we briefly discuss BS to RIS (BS-RIS) and RIS to UE (RIS-UE) channel models. Due to the passive nature of the RIS-elements, the signal transmitted through path **B** suffers from double large-scale pathloss, i.e., $r_1^{-\alpha}$ and $r_2^{-\alpha}$; while profiting from the passive beamforming at the RIS which causes the power of the reflected beam scales up by M^2. Therefore, the received power at the UE through path **B**, denoted by P_u, follows

$$
P_u \propto \frac{P_s}{2} \times \frac{M^2 \lambda^2}{(4\pi)^2 r_1^\alpha r_2^\alpha}, \quad (14)
$$

where λ is the wavelength. Furthermore, by taking the small-scale fading into account for path **B**, the end-to-end channel matrix $\mathbf{H} \in \mathbb{C}^{N \times 1}$ is given by [45]

$$
\mathbf{H} = \mathbf{C}\mathbf{\Phi}\mathbf{D}, \quad (15)
$$

where $\mathbf{C} \in \mathbb{C}^{N \times M}$ and $\mathbf{D} \in \mathbb{C}^{M \times 1}$ are the matrices of channel coefficients for BS-RIS and RIS-UE paths, respectively. Additionally, $\mathbf{\Phi} \in \mathbb{C}^{M \times M}$ represents the diagonal matrix of phase-shift adjustment coefficients of the RIS-reflectors which is associated with the τ_m discussed in the previous subsection. It is noteworthy that the RIS needs the direction of the UE, i.e., φ, in (12) to generate the matrix $\mathbf{\Phi}$. Since the RIS includes a large number of passive elements, it can profit from the angle-of-arrival (AOA) localization technique in [56] to find φ when UE identifies itself by broadcasting the response to the paging message from the associated BS. Moreover, assuming the RIS is equipped with received RF chain, as investigated in [13], [26], the RIS can directly obtain the channel state information (CSI) of BS-RIS and RIS-UE paths to achieve the optimal performance.

C. DISTANCE BETWEEN THE RIS AND THE ASSOCIATED BS

An important quantity is the distance between the engaged RIS and the associated BS, denoted by r_1, which affects the transmit power at the RIS considering the large-scale fading. Although the BSs and RISs are both distributed based on two independent homogeneous PPPs, i.e., Φ_{BS} and Φ_{RIS}, r_1 depends on both r_0 and r_2 as shown in Figure 6. Therefore, the distribution of r_1 for given r_0 and r_2 equals the captured annulus of the circumference of the circle with a radius of r_2 and origin of the UE as shown in Figure 6. Hence, the CDF of r_1 becomes the probability of the engaged RIS
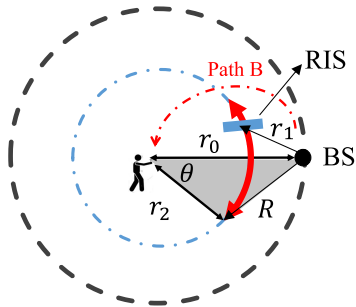
FIGURE 6. The distance between the associated BS and the associated RIS is limited to $|r_0 - r_2| < r_1 < r_0 + r_2$. The red captured annulus indicates where the potential RIS can be located when $r_1 \leqslant R$ for given r_0 and r_2.

located on annulus of $2\theta r_2$ over the whole possible area of the circumference of $2\pi r_2$ as follows:

$$\Pr(r_1 < R|r_0, r_2) = F_{r_1}(R|r_0, r_2) = \frac{2\theta r_2}{2\pi r_2} = \frac{\theta}{\pi}. \quad (16)$$

From the law of Cosines in the shaded triangle,[5] we have

$$\theta = \cos^{-1}\left(\frac{r_0^2 + r_2^2 - R^2}{2r_0 r_2}\right). \quad (17)$$

By substituting (17) in (16) we have

$$F_{r_1}(R|r_0, r_2) = \frac{\cos^{-1}\left(\frac{r_0^2 + r_2^2 - R^2}{2r_0 r_2}\right)}{\pi} \quad (18)$$

Then, the PDF of r_1 for given r_0 and r_2 can be obtained as

$$f_{r_1}(r_1|r_0, r_2) = \frac{dF_{r_1}(r_1)}{dr_1} = \frac{r_1}{\pi r_0 r_2 \sqrt{1 - \left(\frac{r_0^2 + r_2^2 - r_1^2}{2r_0 r_2}\right)^2}}. \quad (19)$$

It is noteworthy that the r_1 can vary from $|r_0 - r_2|$ to $r_0 + r_2$. Eventually, from (1) and (8), the PDF of the r_1 is given by

$$f_{r_1}(r_1) = \int_{r_0=0}^{\infty} \int_{r_2=0}^{\infty} f_{r_1}(r_1|r_2, r_0)f(r_2)f(r_0) \; dr_2 \; dr_0,$$
$$\text{s.t. } |r_0 - r_2| \leqslant r_1 \leqslant r_0 + r_2. \quad (20)$$

Figure 7 shows the theoretical PDF of the r_1 which coincides with the simulation results. In addition, in order to see the impact of λ_{RIS} and λ_{BS} on the r_1, the expected value of r_1 in (20) with putting its condition into the integral becomes

$$\mathbb{E}\{r_1\} = \int_{r_0=0}^{\infty} \int_{r_2=0}^{\infty} \int_{r_1=|r_0-r_2|}^{r_0+r_2} r_1$$
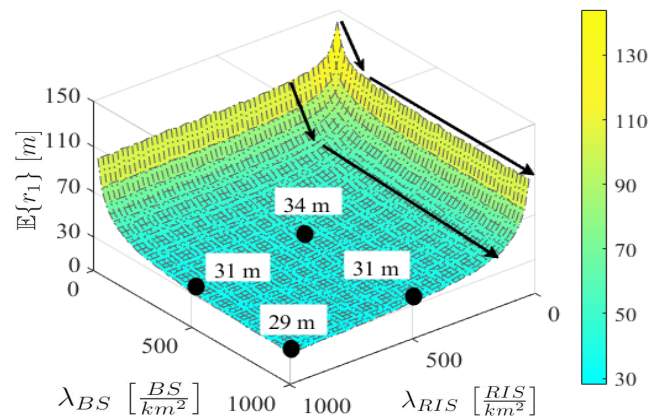$$\times f(r_1|r_2, r_0)f(r_2)f(r_0) \; dr_1 \; dr_2 \; dr_0.$$

Thus, we have

$$\mathbb{E}\{r_1\} = 4\pi \lambda_{BS} \lambda_{RIS} \int_{r_0=0}^{\infty} \int_{r_2=0}^{\infty} \int_{r_1=|r_0-r_2|}^{r_0+r_2} r_1^2$$
$$\times \frac{\exp\left[-\pi\left(\lambda_{RIS} r_2^2 + \lambda_{BS} r_0^2\right)\right]}{\sqrt{1 - \left(\frac{r_0^2 + r_2^2 - r_1^2}{2r_0 r_2}\right)^2}} dr_1 \; dr_2 \; dr_0. \quad (21)$$

[5]$a^2 = b^2 + c^2 - 2bc\cos(\hat{A})$
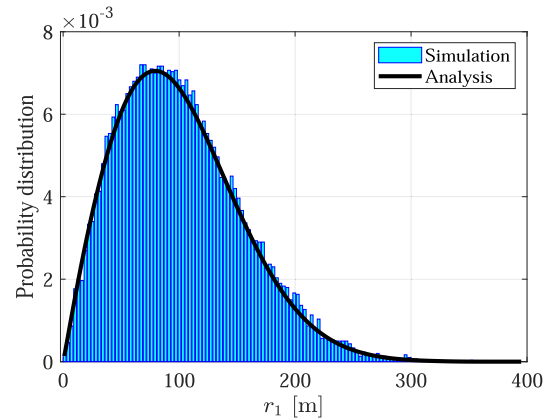
FIGURE 7. Comparison of the analytical and simulation results for the PDF of r_1. $\lambda_{RIS} = 1000 \frac{RIS}{km^2}$, $\lambda_{BS} = 25 \frac{BS}{km^2}$.

**FIGURE 8.** Impact of λ_{RIS} and λ_{BS} on $\mathbb{E}\{r_1\}$.

This integral is numerically calculated using MATLAB as a function of $\mathcal{F}_{r_1}(\lambda_{RIS}, \lambda_{BS}) \triangleq \mathbb{E}\{r_1\}$ which Figure 8 shows its changes when λ_{RIS} and λ_{BS} vary. In general, an increase in either of λ_{RIS} or λ_{BS} reduces $\mathbb{E}\{r_1\}$. For example, for a fixed λ_{BS}, if $\lambda_{RIS_a} < \lambda_{RIS_b}$, then $\mathcal{F}_{r_1}(\lambda_{RIS_a}, \lambda_{BS}) > \mathcal{F}_{r_1}(\lambda_{RIS_b}, \lambda_{BS})$. However, the speed of changes in $\mathcal{F}_{r_1}$ decreases when λ_{RIS} increases. Therefore, we can conclude that from law of large numbers (LLN) theorem, if $\lambda_{RIS_a} < \lambda_{RIS_b}$, $\lambda_{BS_a} < \lambda_{BS_b}$ and $\lambda_{BS_a}, \lambda_{BS_b}, \lambda_{RIS_a}, \lambda_{RIS_b} \rightarrow \infty$, then $\mathcal{F}_{r_1}(\lambda_{RIS_a}, \lambda_{BS_b}) \approx \mathcal{F}_{r_1}(\lambda_{RIS_b}, \lambda_{BS_b})$ in large-scale communications.

D. PEAK REFLECTION SIGNAL POWER OF RIS

The transmitted signal from the associated BS towards the engaged RIS experiences a small-scale fading gain, denoted by f_m, while reaching at the mth RIS-reflector, i.e., from *Assumption 1*, we assume $f_m \sim \exp(\mu)$. Thus, the impinging signal power at the mth passive RIS-reflector is given by

$$\mathcal{P}_m = \frac{P_s}{2} f_m r_1^{-\alpha}. \quad (22)$$

Let us assume an attenuation power factor for RIS-reflectors which is denoted by $\beta \in (0, \; 1]$. Here, β is constant and can be obtained by measuring the attenuation power of a signal passing through the RIS-reflectors. Furthermore, since
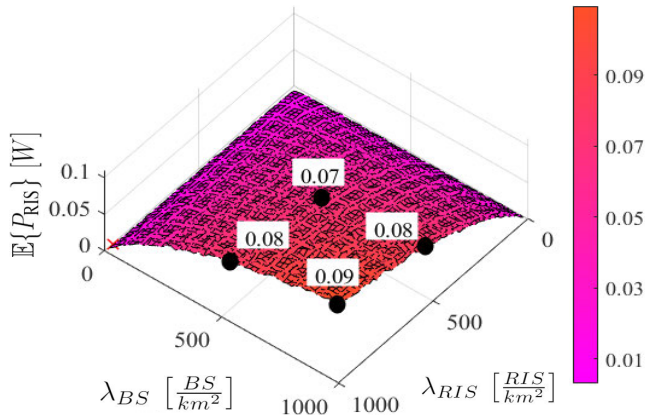
FIGURE 9. Impact of λ_{RIS} and λ_{BS} on average reflected power, i.e., $\mathcal{F}_P\left(\lambda_{RIS}, \lambda_{BS}\right) \triangleq \mathbb{E}\{P_{RIS}\}$, $M = 100$, $\beta = 1$, $\mu = 1$, $\alpha = 4$, and $P_s = 2$ W.

the peak effective radiated power scales up by M^2 as given in (13), the peak reflected power from the engaged RIS towards the UE becomes

$$P_{\text{RIS}} = M^2 \beta \frac{P_s}{2} \mathbb{E}\{f_m\} \, r_1^{-\alpha}. \qquad (23)$$

Consequently the reflected power largely affected by $r_1^{-\alpha}$. With respect to (21), the average peak reflected power can be expressed as a function of λ_{RIS} and λ_{BS} for given α, β and M as follows

$$\mathcal{F}_P\left(\lambda_{RIS}, \lambda_{BS}\right) \triangleq \mathbb{E}\{P_{\text{RIS}}\} = \frac{M^2 \beta P_s}{2\mu} \mathbb{E}\{r_1^{-\alpha}\}, \qquad (24)$$

which is shown in Figure 9. In other words, the dependency of average power on λ_{RIS} and λ_{BS} comes from $\tilde{\mathcal{F}}_{r_1}\left(\lambda_{RIS}, \lambda_{BS}\right) \triangleq \mathbb{E}\{r_1^{-\alpha}\}$ with respect to the PDF of r_1 in (20) and (21). Thus, we conclude that in general, since α is positive, i.e., usually $\alpha > 2$ [3], the average reflected power from the RIS increases when λ_{RIS} increases, i.e., $\mathbb{E}\{r_1\}$ decreases. For example, keeping λ_{BS} fixed, if $\lambda_{RIS_a} < \lambda_{RIS_b}$, then $\mathcal{F}_P\left(\lambda_{RIS_a}, \lambda_{BS}\right) < \mathcal{F}_P\left(\lambda_{RIS_b}, \lambda_{BS}\right)$. Likewise, the reflected power from the RIS decreases when BS density decreases as shown in Figure 9. However, this reflected power reduction can be compensated by employing larger RISs with more number of reflectors, i.e., a larger M.

In order to find the SIR coverage probability of the RIS-assisted path, i.e., path **B**, and simplify the analysis in section IV, we introduce a raw moment of $\left(\frac{P_{\text{RIS}}}{\mu}\right)^{\frac{2}{\alpha}}$ which is calculated as follows:

$$\mathbb{E}\left\{\left(\frac{P_{\text{RIS}}}{\mu}\right)^{\frac{2}{\alpha}}\right\} = \left[\frac{M^2 \beta P_s}{2\mu}\right]^{\frac{2}{\alpha}} \mathbb{E}\left\{f_m^{\frac{2}{\alpha}}\right\} \mathbb{E}\left\{r_1^{-2}\right\}. \quad (25)$$

Since $f_m \sim \exp(\mu)$, we have

$$\mathbb{E}\left\{f_m^{\frac{2}{\alpha}}\right\} = \int_{f_m=0}^{\infty} f_m^{\frac{2}{\alpha}} \mu e^{-\mu f_m} \, df_m = \mu^{-\frac{2}{\alpha}} \Gamma\left(\frac{2}{\alpha}\right), \quad (26)$$

where $\Gamma(x) = \int_0^\infty t^{x-1} e^{-t} \, dt$ is the Gamma function. Moreover, from (20), we define

$$\mathcal{F}_R\left(\lambda_{RIS}, \lambda_{BS}\right) \triangleq \mathbb{E}\left\{r_1^{-2}\right\} = \int_{r_1=\varepsilon}^{\infty} r_1^{-2} f_{r_1}(r_1) \, dr_1, \quad (27)$$

where $\varepsilon = \max\left(|r_0 - r_2|, \epsilon\right)$ and ϵ is a minimum euclidean distance of the BS from the RIS that prevents the divergence of $\mathbb{E}\left\{r_1^{-2}\right\}$. Eventually, by substituting (26) and (27) in (25), we have

$$\mathbb{E}\left\{\left(\frac{P_{\text{RIS}}}{\mu}\right)^{\frac{2}{\alpha}}\right\} = \left[\frac{M^2 \beta P_s}{2\mu^2}\right]^{\frac{2}{\alpha}} \Gamma\left(\frac{2}{\alpha} + 1\right) \mathcal{F}_R\left(\lambda_{RIS}, \lambda_{BS}\right). \qquad (28)$$

Remark 1: The raw moment of $\left(\frac{P_{\text{RIS}}}{\mu}\right)^{\frac{2}{\alpha}}$ in (28) depends on $\mathcal{F}_R\left(\lambda_{RIS}, \lambda_{BS}\right)$ for given α, M, μ and β. Therefore, similar to the $\mathcal{F}_P\left(\lambda_{RIS}, \lambda_{BS}\right) \triangleq \mathbb{E}\{P_{\text{RIS}}\}$ shown in Figure 9, $\mathbb{E}\left\{\left(\frac{P_{\text{RIS}}}{\mu}\right)^{\frac{2}{\alpha}}\right\}$ is an increasing function of λ_{RIS} and λ_{BS}.

IV. SIR COVERAGE PROBABILITY IN RIS-ASSISTED mmWave CELLULAR NETWORK

In order to facilitate the UE implementation for the receptions through two paths **A** and **B** at the receiver, diversity is taken into account. By selection diversity of two received signals, the strongest signal is selected. Let Γ_A, and Γ_B denote the SIRs of the received signals through paths **A** and **B**, respectively. Then, the SIR at the UE is given by

$$\Gamma_s = \max\{\Gamma_A, \Gamma_B\}. \qquad (29)$$

The SIR of the received signal from path **A** is similar to the baseline model while the beamwidth and transmit signal power at the active BS are being affected, i.e., $\psi_s = \sqrt{2}\psi_o$ and $\frac{P_s}{2}$ in 2D space. Consequently, the co-channel interference is affected as an additional gain of beamforming and the interferer BSs density becomes

$$\lambda_{I_s} = \sqrt{\frac{2}{N}} \lambda_{BS}. \qquad (30)$$

Therefore, taking these changes into account and similar to (6), the SIR coverage probability for path **A** can be obtained as

$$\Pr\left[\Gamma_A > T\right] = \frac{1}{\left(1 + \sqrt{\frac{2}{N}} T^{\frac{2}{\alpha}} \int_{T^{-\frac{2}{\alpha}}}^{\infty} \frac{1}{1+u^{\frac{\alpha}{2}}} du\right)}. \qquad (31)$$

On the other hand, the SIR of the received signal through path **B** is given by

$$\Gamma_B = \frac{P_{\text{RIS}} h r_2^{-\alpha}}{\displaystyle\sum_{\substack{BS_i \in \Phi_I, \\ i \neq 0}} \frac{P_s}{2} g_i r_i^{-\alpha}}, \qquad (32)$$

where h denotes the small-scale fading gain between the engaged RIS and the UE. Based on *Assumption 1* we have $h \sim \exp(\mu)$. In order to simplify the analysis to find a closed-form expression for $\Pr\{\Gamma_B > T\}$, we utilize the following conversion.

Remark 2 (Power-Density Conversion): The path-loss process of $r \in \Phi$ with transmit power P and intensity λ is

equivalent with that of $\mathcal{R} \in \tilde{\Phi}$ with a transmit power of 1 and an intensity of $\tilde{\lambda}$ given as

$$\tilde{\lambda} = P^{\frac{2}{\alpha}} \lambda. \tag{33}$$

The proof of this *remark* is similar to that of [59, lemma 1]. However, for the reader's convenience, a simplified version is provided in Appendix 65.

Therefore based on *remark 2*, we have $\Phi_{BS} \rightarrow \tilde{\Phi}_{BS}$, $\Phi_I \rightarrow \tilde{\Phi}_I$ and $\Phi_{RIS} \rightarrow \tilde{\Phi}_{RIS}$; and from (32), the SIR coverage probability for path **B** is given by

$$Pr\{\Gamma_B > T\} = \mathbb{E}\left\{Pr\left(\frac{\tilde{h}r_2^{-\alpha}}{\sum\limits_{\substack{BS_i \in \tilde{\Phi}_I, \\ i \neq 0}} \tilde{g}_i r_i^{-\alpha}} > T\right)\right\}, \tag{34}$$

where

$$\tilde{\lambda}_{BS} = \left(\frac{P_s}{2\mu}\right)^{\frac{2}{\alpha}} \lambda_{BS} \tag{35}$$

$$\tilde{\lambda}_I = \left(\frac{P_s}{2\mu}\right)^{\frac{2}{\alpha}} \lambda_{Is} \tag{36}$$

$$\tilde{\lambda}_{RIS} = \mathbb{E}\left\{\left(\frac{P_{RIS}}{\mu}\right)^{\frac{2}{\alpha}}\right\} \lambda_{RIS}, \tag{37}$$

$$\tilde{g}_i \sim \exp(1) \quad \text{and} \quad \tilde{h} \sim \exp(1). \tag{38}$$

By taking the changes in (35) to (38) into account, the SIR coverage probability in (34) becomes

$$Pr\{\Gamma_B > T\} = \mathbb{E}\left\{Pr\left(\tilde{h} > Tr_2^\alpha \sum_{BS_i \in \tilde{\Phi}_I} \tilde{g}_i r_i^{-\alpha}\right)\right\}. \tag{39}$$

Since $\tilde{h} \sim \exp(1)$ and $Pr(\tilde{h} > x) = 1 - F_{\tilde{h}}(x) = e^{-x}$, (39) becomes

$$Pr\{\Gamma_B > T\} = \mathbb{E}\left\{\exp\left(-Tr_2^\alpha \sum_{BS_i \in \tilde{\Phi}_I} \tilde{g}_i r_i^{-\alpha}\right)\right\}$$

$$= \mathbb{E}\left\{\prod_{BS_i \in \tilde{\Phi}_I} \exp\left(-T\tilde{g}_i \left[\frac{r_2}{r_i}\right]^\alpha\right)\right\}. \tag{40}$$

Since $\tilde{g}_i \sim \exp(1)$, we have $\mathbb{E}\left\{e^{-\tilde{g}_i x}\right\} = [1+x]^{-1}$ and (40) becomes

$$Pr\{\Gamma_B > T\} = \mathbb{E}\left\{\prod_{BS_i \in \tilde{\Phi}_I} \frac{1}{1+T\left[\frac{r_2}{r_i}\right]^\alpha}\right\}. \tag{41}$$

With simplification by application of Campbell's theorem [46], [54], [60],[6] from (41) we have

$$\mathbb{E}\left\{\prod_{BS_i \in \tilde{\Phi}_I} \frac{1}{1+T\left[\frac{r_2}{r_i}\right]^\alpha}\right\}$$

[6]$\mathbb{E}\left\{\prod\limits_{x \in \tilde{\Phi}_I} f(x)\right\} = \exp\left[-\tilde{\lambda}_I \int_{\mathbb{R}^2}(1-f(x))dx\right].$

$$= \mathbb{E}\left\{\exp\left(-2\pi\tilde{\lambda}_I \int_{\upsilon=r_0}^\infty \left[1 - \frac{1}{1+T\left[\frac{r_2}{\upsilon}\right]^\alpha}\right]\upsilon d\upsilon\right)\right\}. \tag{42}$$

Simplifying the integral expression in (42) is a complicated task since the lower bound in integral is a function of r_0 and the expression inside the integral is a function of r_2 which are independent of each other. To simplify (42) and find a closed-form expression for Γ_B coverage probability, at this stage, we provide two approximations as follows.

A. APPROXIMATION-I
In this approximation, from (1) and (8), we have

$$\mathbb{E}\{r_{2,0}\} = \sqrt{\frac{\tilde{\lambda}_{BS}}{\tilde{\lambda}_{RIS}}} \mathbb{E}\{r_0\} \tag{43}$$

Therefore, we simply approximate

$$r_2 \approx \rho r_0, \tag{44}$$

where $\rho = \sqrt{\frac{\tilde{\lambda}_{BS}}{\tilde{\lambda}_{RIS}}}$. Consequently we define the following *proposition*.

Proposition 1: The SIR coverage probability for path **B** of a randomly located UE in RIS-assisted mmWave cellular network with **Approximation I** is

$$Pr\{\Gamma_B > T\} = \frac{\tilde{\lambda}_{RIS}}{\tilde{\lambda}_{RIS} + \frac{\tilde{\lambda}_I}{\rho^2}(T)^{\frac{2}{\alpha}} \int_{u=(T)^{-\frac{2}{\alpha}}}^\infty \frac{\rho^\alpha}{\rho^\alpha + u^{\frac{\alpha}{2}}} du} \tag{45}$$

Proof: By Taking (44) into account, (42) becomes

$$\mathbb{E}\left\{\exp\left(-2\pi\tilde{\lambda}_I \int_{\upsilon=\frac{r_2}{\rho}}^\infty \left[1 - \frac{1}{1+T\left[\frac{r_2}{\upsilon}\right]^\alpha}\right]\upsilon d\upsilon\right)\right\} \tag{46}$$

By employing a change of variable $u = \frac{\rho^2 \upsilon^2}{r_2^2 (T)^{\frac{2}{\alpha}}}$, we have

$$\mathbb{E}\left\{\exp\left(-\frac{\pi\tilde{\lambda}_I (T)^{\frac{2}{\alpha}} r_2^2}{\rho^2} \int_{u=(T)^{-\frac{2}{\alpha}}}^\infty \frac{\rho^\alpha}{\rho^\alpha + u^{\frac{\alpha}{2}}} du\right)\right\} \tag{47}$$

By taking the average of (47) over r_2 with respect to (8) and (37), we have

$$\int_{r_2=0}^\infty f_{r_2}(r_2) \exp$$
$$\times \left(-\frac{\pi\tilde{\lambda}_I (T)^{\frac{2}{\alpha}} r_2^2}{\rho^2} \times \int_{u=(T)^{-\frac{2}{\alpha}}}^\infty \frac{\rho^\alpha}{\rho^\alpha + u^{\frac{\alpha}{2}}} du\right) dr_2. \tag{48}$$

Let consider parameter $\mathcal{J}$ as follows

$$\mathcal{J} = \pi\left(\tilde{\lambda}_{RIS} + \frac{\tilde{\lambda}_I}{\rho^2}(T)^{\frac{2}{\alpha}} \int_{u=(T)^{-\frac{2}{\alpha}}}^\infty \frac{\rho^\alpha}{\rho^\alpha + u^{\frac{\alpha}{2}}} du\right). \tag{49}$$

Then, (48) becomes

$$Pr\{\Gamma_B > T\} = 2\pi\tilde{\lambda}_{RIS} \int_{r_2=0}^\infty r_2 e^{-\mathcal{J}r_2^2} dr_2 = \frac{\pi\tilde{\lambda}_{RIS}}{\mathcal{J}} \tag{50}$$

Eventually by substituting $\mathcal{J}$ in (49) into (50) we have

$$Pr\left\{\Gamma_B > T\right\} = \frac{\tilde{\lambda}_{RIS}}{\tilde{\lambda}_{RIS} + \frac{\tilde{\lambda}_I}{\rho^2}(T)^{\frac{2}{\alpha}} \int_{u=(T)^{-\frac{2}{\alpha}}}^{\infty} \frac{\rho^{\alpha}}{\rho^{\alpha}+u^{\frac{\alpha}{2}}}du}$$

■

B. APPROXIMATION-II

In this approximation we consider a lower bound where $\lambda_{RIS} \gg \lambda_{BS} \rightarrow \upsilon \geqslant r_2$ in (42). Therefore, we state the following *proposition*.

Proposition 2: The lower bound SIR coverage probability for path **B** of a randomly located UE in RIS-assisted mmWave cellular network when $\lambda_{RIS} \gg \lambda_{BS}$ with **Approximation II** is

$$\Pr\left\{\Gamma'_B > T\right\} = \frac{\tilde{\lambda}_{RIS}}{\tilde{\lambda}_{RIS} + \tilde{\lambda}_I(T)^{\frac{2}{\alpha}} \int_{u=(T)^{-\frac{2}{\alpha}}}^{\infty} \frac{1}{1+u^{\frac{\alpha}{2}}}du} \quad (51)$$

Proof: Since the proof is similar to that in *proposition 1*, we omit it here.

■

V. DISCUSSION ON BASELINE AND RIS-ASSISTED mmWave CELLULAR NETWORKS

The SIR coverage probability of the baseline model in (6) and path **A** in the RIS-assisted model in (31) does not depend on λ_{BS}; and the only deployment parameter to enhance the SIR performance is N which means that with $N \rightarrow \infty$, we have

$$N \rightarrow \infty \Rightarrow \begin{cases} \Pr\left\{\Gamma_o > T\right\} \rightarrow 1 \\ \Pr\left\{\Gamma_A > T\right\} \rightarrow 1 \end{cases}. \quad (52)$$

However the lower bound SIR probability in (51) in **Approximation II** shows that the SIR performance for path **B** depends on deployment parameters of not only N but also λ_{BS}, λ_{RIS}, and M. In other words, from (28) and (37), (51) can be re-expressed as

$$\Pr\left\{\Gamma'_B > T\right\}$$
$$= \frac{\lambda_{RIS}M^{\frac{4}{\alpha}}\mathcal{F}_1(\lambda_{BS}, \lambda_{RIS}, \alpha, \beta)}{\lambda_{RIS}M^{\frac{4}{\alpha}}\mathcal{F}_1(\lambda_{BS}, \lambda_{RIS}, \alpha, \beta) + \sqrt{\frac{2}{N}}\lambda_{BS}\mathcal{F}_2(T, \alpha)}, \quad (53)$$

where

$$\begin{cases} \mathcal{F}_1(\lambda_{BS}, \lambda_{RIS}, \alpha, \beta) = \left[\frac{\beta}{\mu}\right]^{\frac{2}{\alpha}} \Gamma\left(\frac{2}{\alpha}+1\right)\mathcal{F}_R(\lambda_{RIS}, \lambda_{BS}) \\ \mathcal{F}_2(T, \alpha) = (T)^{\frac{2}{\alpha}} \int_{u=(T)^{-\frac{2}{\alpha}}}^{\infty} \frac{1}{1+u^{\frac{\alpha}{2}}}du \end{cases}$$

Based on *remark 1*, $\mathcal{F}_R$ and consequently $\mathcal{F}_1$ are increasing functions of λ_{RIS}. Therefore, we have

$$\left.\begin{matrix} \lambda_{RIS} \rightarrow \infty \\ or \ M \rightarrow \infty \\ or \ N \rightarrow \infty \end{matrix}\right\} \Rightarrow \Pr\left\{\Gamma'_B > T\right\} \rightarrow 1. \quad (54)$$

Nevertheless, in practice, there are implementation issues which might prevent these parameters to become very large. However, there is a great deal of flexibility to select a proper parameter for SIR enhancement. For instance, a lower complex antenna array, i.e., smaller N, can be deployed at

TABLE 1. System numerical parameters.

System parameters	Corresponding value
BS radiated power (downlink) , P_s	2 W
BS antenna array, N	16 antennas
RIS elements, M	100 reflectors
Attenuation power ratio at RIS-elements, β	0.9
Channel bandwidth, W	100 MHz
Pathloss exponent, α	4
Small-scale channel gain of BS-UE under the ISO antenna model [47]	$g_i \sim \exp\left(\frac{0.827}{(8)^{0.927}}\right)$
Small-scale channel gain of BS-RIS under the ISO antenna model [47]	$f_m \sim \exp\left(\frac{0.827}{(8 \times 100)^{0.927}}\right)$
Small-scale channel gain of RIS-UE under the ISO antenna model [47]	$h \sim \exp\left(\frac{0.827}{(100)^{0.927}}\right)$
Noise floor power	-94 dBm

the BS and either higher RIS density or larger number of reflectors M can be taken into account to provide a desired SIR gain. On the other hand, from (53) and in large BS densities when λ_{BS} increases, although the $\mathcal{F}_1$ in the numerator increases, the expression in the denominator increases faster than the numerator because of additive expression of $\sqrt{\frac{2}{N}}\lambda_{BS}\mathcal{F}_2(T, \alpha)$. In other words, the co-channel interference increases faster than the reflected power from the RIS when the active BS density increases, i.e.,

$$\Pr\left\{\Gamma'_B > T\right\} \propto \frac{C_1\lambda_{RIS}}{C_1\lambda_{RIS} + C_2\lambda_{BS}}, \quad (55)$$

where C_1 and C_2 are assumed to be constant for specific moments. Therefore, it is desirable to decrease the number of active BSs (only when λ_{BS} is large and background noise at the UE is negligible) and deploy more passive RISs. Note that this is only applicable in large λ_{BS} where the background noise at the UE is negligible compared to the received interference signal power. In other words, although BS density decrement improves the SIR performance in large BS densities, the BS density cannot be too small since the performance might be affected by the background noise at the UE. In such a case, SIR cannot be a reliable metric and analysis should be applied to the SINR performance which its analysis in more details is out of the scope of this study.

VI. NUMERICAL RESULTS

In this section, the performance of the RIS-assisted is shown by simulation results. The evaluations include: A) the SIR coverage probability comparison for both paths **A** and **B** in the RIS-assisted model, B) the SIR coverage probability comparison of the RIS-assisted and the baseline models, and C) the impact of λ_{RIS} and λ_{BS} on SIR coverage probability.

We use MATLAB and the parameters used in the simulations are given in TABLE 1, unless otherwise specified.

A. SIR COVERAGE EVALUATION IN RIS-ASSISTED MODEL

Since the selection diversity of the two received signals is taken into account in the proposed RIS-assisted model,
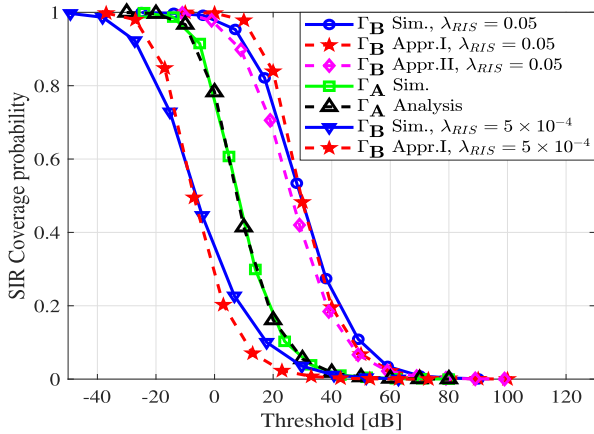
FIGURE 10. Coverage evaluation of the RIS-assisted model through paths A and B. RIS densities are in $\frac{RIS}{m^2}$, $\lambda_{BS} = 2.5 \times 10^{-5} \frac{BS}{m^2}$, and $M = 100$.

FIGURE 11. Coverage comparison between the RIS-assisted and the baseline models. RIS densities are in $\frac{RIS}{m^2}$. $\lambda_{BS} = 2.5 \times 10^{-5} \frac{BS}{m^2}$.

the UE is able to select the strongest signal between those received signals through paths **A** and **B**. Figure 10 compares the SIR coverage probabilities for both of paths *A* and **B**. Based on (31), (45) and (51), Γ_A only depends on N while Γ_B depends on λ_{RIS} as well. Therefore, it is shown that when λ_{RIS} increases from 5×10^{-4} to 0.05 $\frac{RIS}{m^2}$, Γ_B is improved. Moreover, when λ_{RIS} becomes larger, i.e., $\lambda_{RIS} \gg \lambda_{BS}$, Γ_B outperforms Γ_A.

## B. SIR COMPARISON OF RIS-ASSISTED AND BASELINE MODELS

Figure 11 compares the the coverage performance of the proposed model with the baseline model. It shows that there is a minimum coverage probability when there is no RIS-assisted path between the BS and the UE, i.e., small λ_{RIS} results in $\Gamma_s = \Gamma_A$ which is independent of λ_{RIS}, e.g., $\lambda_{RIS} = 10^{-5} \frac{RIS}{m^2}$. This minimum coverage probability is slightly less than that of the baseline model since we have two beams in the RIS assisted model while there is only one beam in the baseline model with the same BS structure. In other words, with fixed N active antennas at the BSs, the beam in the baseline model is narrower that that of the RIS-assisted model causes less co-channel interference. However, when λ_{RIS} increases, the coverage probability in the RIS-assisted is improved. In addition, bigger RISs, i.e., a larger M, performs better than small RISs as it increases the reflected power from the engaged RIS. On the other hand, in such a case where there might be an infeasibility of high RIS density deployment, larger M can be taken into account to provide the required SIR improvement.

C. IMPACT OF λ_{RIS} AND λ_{BS} ON SIR COVERAGE PERFORMANCE

Figure 12 shows the impact of λ_{RIS} on the proposed RIS-assisted model. As discussed in section V, when λ_{RIS} increases, the SIR coverage probability of Γ_B approaches 1. Moreover, we can see that **Approximation I** is supported by the simulation results in high λ_{RIS} because when $\lambda_{RIS} \to \infty$,
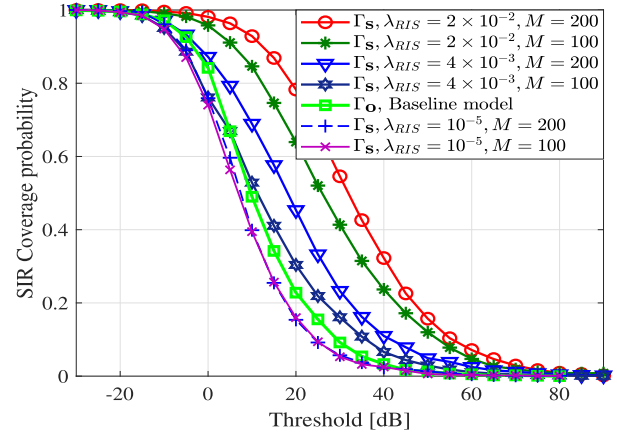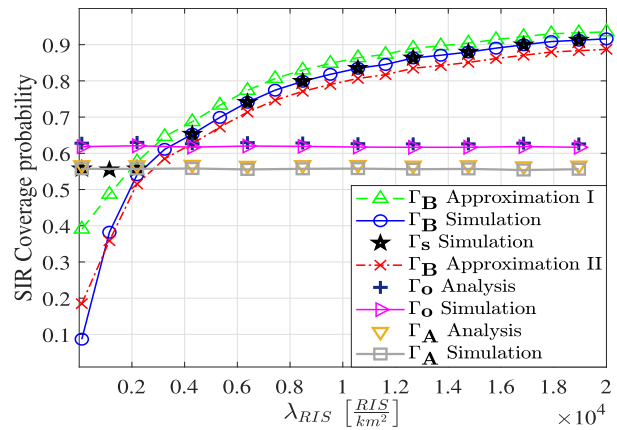

FIGURE 12. Impact of λ_{RIS} on SIR coverage performance. $\lambda_{BS} = 2.5 \times 10^{-5} \frac{BS}{m^2}$, $M = 100$ and $T = 5$ dB.

the distance of r_2 and its variations becomes smaller; therefore, $r_2 \approx \rho r_0$ in (44) becomes more realistic. In addition, the SIR performances for the baseline model and the path **A** in the RIS-assisted model are fixed and independent from the λ_{RIS} variations. Γ_o has better performance compared to Γ_A due to having a narrower beamwidth since it uses all N elements to create one beam while in the proposed model there are two wider beams with the same BS structure. Figure 13 depicts the SIR coverage performance of the RIS-assisted and the baseline model with respect to λ_{BS}. As λ_{BS} increases, Γ_o and Γ_A remain unchanged while Γ_B slightly decreases. It shows that although higher λ_{BS} leads to a higher reflected power from the RIS, its impact on the co-channel interference power is larger. In other words, the speed of increasing of co-channel interference power is faster than that of reflected power from the RIS. However, it is noteworthy that the simulation results shown in Figure 13 are for large BS densities, i.e., $\lambda_{BS} > 25 \frac{BS}{km^2}$ and the background noise at the UE is negligible compared to the received interference power. But Figure 14 shows the results for similar simulation when SINR coverage probability is taken into account with a noise floor of -94 dBm and small λ_{BS} values are
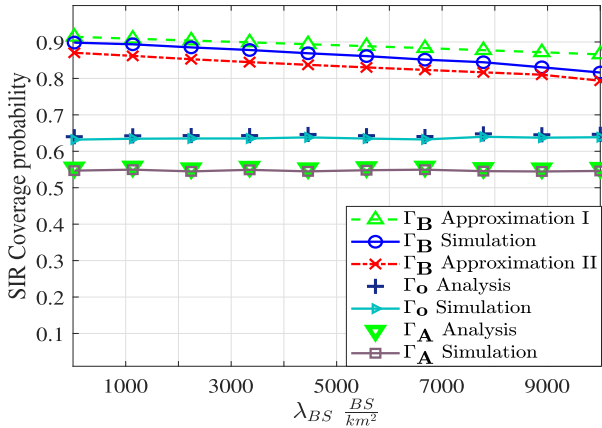
FIGURE 13. Impact of λ_{BS} on SIR coverage performance. $\lambda_{RIS} = 2 \times 10^{-2} \frac{RIS}{m^2}$ and $T = 5$ dB.
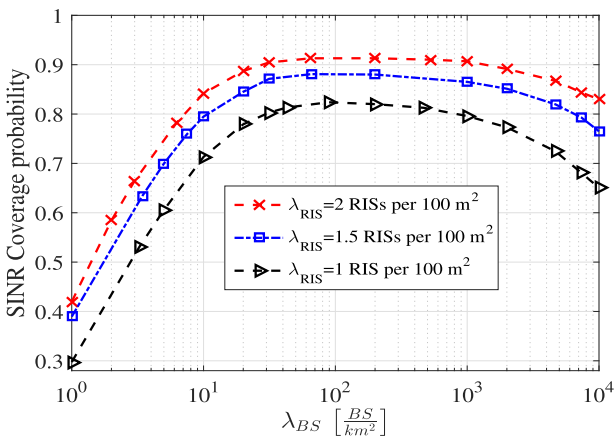
FIGURE 14. SINR performance evaluation of the proposed model with respect to the λ_{BS} when λ_{RIS} varies from $10\,000 \frac{RIS}{km^2}$ to $20\,000 \frac{RIS}{km^2}$ and $T = 5$ dB.

shown in the logarithmic x-axis. In other words, it shows that although in high BS densities, smaller λ_{BS} has better performance, there is a trade-off when the λ_{BS} decreases significantly.

Considering both simulation results in Figures 13 and 14, we note the feasibility of our analysis in the high BS density regime even for SINR. Nevertheless, the difference under the low BS density regime calls for further investigation on SINR analysis in future research.

Recent studies [44], [57] also confirm the same conclusion that the coverage performance improves after exceeding a certain ratio of RIS to BS. This critical RIS/BS ratio threshold depends highly on the system configurations and simulation parameters (e.g., the numbers of RIS-reflectors and BS antennas, channel models, etc.), and investigating on finding the specific values. Moreover, In [44], it was shown that compared to the conventional active relaying, RIS requires much lower hardware cost and energy consumption due to passive reflection, and works spectral efficiently in full-duplex without the need of costly self-interference cancellation techniques [44]. In addition, it was discussed that the RIS-aided system outperforms the full-duplex relaying based

system in terms of the spatial throughput as the number of RIS-reflectors increases [44].

VII. CONCLUSION
In this study, we proposed a new RIS-assisted mmWave cellular network where a message is transmitted by a BS towards a desired UE though two LoS and NLoS paths. The NLoS path passes through an RIS and then, reflected towards the UE. Discrete time delay values corresponding the phase-shifts at each RIS-reflector was elaborated and the peak reflection power at the RIS was assessed. Since the UE utilizes selection diversity technique to pick the strongest signal received through the two paths, we analysed the SIR coverage performance of both paths with major emphasis on RIS and BS densities and compared its performance with a baseline model. Two closed-form approximations were derived analytically for the SIR coverage probability of the RIS-assisted path. It was shown that the SIR coverage probability of the RIS-assisted path depends on not only N but also λ_{RIS}, λ_{BS}, and M which provides a great deal of flexibility to obtain a desired SIR gain. Furthermore, we note that the density magnitudes seem to be large numbers. Nevertheless, the RIS concept is supposed to be taken into action in 6G and in this proposed network model there are some assumptions related to the considered system model to show the general performance of the system while practicality feasibility of such implementations is more relevant to the commercial value of the proposed method. Besides, it is also noteworthy that massive MIMO concept, and recently proposed radio stripes patented in 2017 [61] or even holographic beam-forming proposed in the 90's [62], [63] can help and support the technical and commercial implementation of such surfaces.

APPENDIX A
DERIVATION OF Pr[$\Gamma_o > T$]
Similar to the analysis in [46], the SIR coverage probability in (5) becomes

$$\Pr[\Gamma_o > T]$$

$$= \underset{\substack{g_0 \\ g_i \\ r_i \\ r_0}}{\mathbb{E}} \left\{ \Pr\left(g_0 > T r_0^\alpha \sum_{\substack{BS_i \in \Phi_I \\ i \neq 0}} g_i r_i^{-\alpha} \right) \right\}$$

$$= \underset{\substack{g_i \\ r_i \\ r_0}}{\mathbb{E}} \left\{ \exp\left(-\mu T r_0^\alpha \sum_{\substack{BS_i \in \Phi_I \\ i \neq 0}} g_i r_i^{-\alpha} \right) \right\}$$

$$= \underset{\substack{r_i \\ r_0}}{\mathbb{E}} \left\{ \prod_{\substack{BS_i \in \Phi_I \\ i \neq 0}} \underset{g_i}{\mathbb{E}} \left\{ \exp\left(-\mu g_i T \left[\frac{r_0}{r_i} \right]^\alpha \right) \right\} \right\}$$

$$\overset{\mathbb{E}\{e^{-g_i x}\} = \mu[\mu+x]^{-1}}{=} \underset{r_0}{\mathbb{E}} \left\{ \underset{r_i}{\mathbb{E}} \left\{ \prod_{\substack{BS_i \in \Phi_I \\ i \neq 0}} \mu \left(\mu + \mu T \left[\frac{r_0}{r_i} \right]^\alpha \right)^{-1} \right\} \right\}$$

$$
\overset{\text{Campbell's theorem}}{=} \underset{r_0}{\mathbb{E}} \left\{ \exp\left(-2\pi\lambda_I 5 \int_{\upsilon=r_0}^{\infty} \left[1 - \left(1 + T\left[\frac{r_0}{\upsilon}\right]^\alpha\right)^{-1} \right] \upsilon d\upsilon \right) \right\}.
$$
(56)

With changing the variable as $u = \frac{\upsilon^2}{r_0^2 (T)^{\frac{2}{\alpha}}}$ and averaging over r_0, we have

$$
\Pr[\Gamma_o > T] =
$$
$$
\int_{r_0=0}^{\infty} f_{r_o}(r_0) \exp\left(-\pi\lambda_I r_0^2 (T)^{\frac{2}{\alpha}} \int_{u=(T)^{-\frac{2}{\alpha}}}^{\infty} \frac{1}{1+u^{\frac{\alpha}{2}}} du \right) d r_0. \quad (57)
$$

Eventually, the closed form of (57) becomes

$$
\Pr[\Gamma_o > T] = \frac{\lambda_{BS}}{\left(\lambda_{BS} + \lambda_I T^{\frac{2}{\alpha}} \int_{T^{-\frac{2}{\alpha}}}^{\infty} \frac{1}{1+u^{\frac{\alpha}{2}}} du \right)}
$$
$$
\overset{\lambda_I=\frac{\lambda_{BS}}{\sqrt{N}}}{=} \frac{1}{\left(1 + \frac{1}{\sqrt{N}} T^{\frac{2}{\alpha}} \int_{T^{-\frac{2}{\alpha}}}^{\infty} \frac{1}{1+u^{\frac{\alpha}{2}}} du \right)}. \quad (58)
$$

APPENDIX B
DERIVATION OF $f_{r_2}(r|r_2 < r_0)$

Since, the BSs and RISs are independently distributed in the area and utilizing Bayes theorem, the CDF of being $r_2 < r_0$ is given by

$$
F_{r_2}(R|r_2 < r_0) = \frac{\int_{r_2=0}^{R} \Pr(r_0 > r_2|r_2) f_{r_2}(r_2) dr_2}{F_{r_2}(r_0)}. \quad (59)
$$

From (1) and (8), the numerator of (59) becomes

$$
\int_{r_2=0}^{R} \left[e^{-\pi\lambda_{BS} r_2^2} \right] f_{r_2}(r_2) dr_2 = \frac{\lambda_{RIS}}{\lambda_{BS} + \lambda_{RIS}}
$$
$$
\times \left[1 - e^{-\pi(\lambda_{RIS}+\lambda_{BS})R^2} \right]. \quad (60)
$$

Then, the denominator of (59) becomes

$$
F_{r_2}(r_0) = \Pr[r_2 < r_0]
$$
$$
= \int_{r_0=0}^{\infty} \left[\int_{r_2=0}^{r_0} f_{r_2}(r_2) dr_2 \right] f_{r_0}(r_0) dr_0
$$
$$
= \frac{\lambda_{RIS}}{\lambda_{BS} + \lambda_{RIS}}. \quad (61)
$$

Eventually, by substituting (60) and (61) into (59), we have

$$
F_{r_2}(R|r_2 < r_0) = 1 - e^{-\pi(\lambda_{RIS}+\lambda_{BS})R^2}. \quad (62)
$$

Consequently, we have

$$
f_{r_2}(r|r_2 < r_0) = 2\pi(\lambda_{RIS} + \lambda_{BS}) r e^{-\pi(\lambda_{RIS}+\lambda_{BS})r^2}.
$$

The analysis is complete.

APPENDIX C
POWER-DENSITY CONVERSION

Let $r = \sqrt{x^2 + y^2}$ and $x, y \in \Phi$ (homogeneous PPP) with intensity of λ in the 2-dimensional Euclidean plane. Similarly, let also consider a new r.v. $\mathcal{R} = \sqrt{\mathcal{X}^2 + \mathcal{Y}^2}$ where $\mathcal{X}, \mathcal{Y} \in \tilde{\Phi}$ with intensity of $\tilde{\lambda}$. Suppose constant values of P and α where we have

$$
\mathcal{R}^{-\alpha} = Pr^{-\alpha} = \left[(P)^{-\frac{1}{\alpha}} r \right]^{-\alpha}
$$
$$
= \left[\sqrt{ \underbrace{(P)^{-\frac{2}{\alpha}} x^2}_{\mathcal{X}} + \underbrace{(P)^{-\frac{2}{\alpha}} y^2}_{\mathcal{Y}} } \right]^{-\alpha}. \quad (63)
$$

Therefore, we have

$$
\begin{bmatrix} \mathcal{X} \\ \mathcal{Y} \end{bmatrix} = \overbrace{\begin{bmatrix} P^{-\frac{1}{\alpha}} & 0 \\ 0 & P^{-\frac{1}{\alpha}} \end{bmatrix}}^{A} \begin{bmatrix} x \\ y \end{bmatrix}. \quad (64)
$$

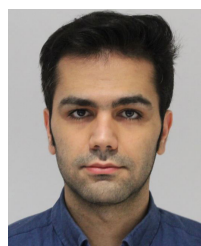Consequently, profiting from mapping theorem, we can conclude $\Phi \to \tilde{\Phi}$ where

$$
\tilde{\lambda} = \det[A^{-1}]\lambda = P^{\frac{2}{\alpha}}\lambda. \quad (65)
$$

REFERENCES

[1] GSM Association (GSMA), "White paper: Study on socio-economic benefits of 5G services provided in mmWave bands," Roscongress, London, U.K., Tech. Rep., Dec. 2018. [Online]. Available: https://www.gsma.com/spectrum/wp-content/uploads/2019/10/mmWave-5G-benefits.pdf

[2] Ericsson Inc., "White Paper: Ericsson mobility report June 2019," Ericsson, Stockholm, Sweden, Tech. Rep., Jun. 2019. [Online]. Available: https://www.ericsson.com/en/mobility-report/reports

[3] S. Rangan, T. S. Rappaport, and E. Erkip, "Millimeter-wave cellular wireless networks: Potentials and challenges," *Proc. IEEE*, vol. 102, no. 3, pp. 366–385, Mar. 2014.

[4] J. Ding, M. Nemati, C. Ranaweera, and J. Choi, "IoT connectivity technologies and applications: A survey," *IEEE Access*, vol. 8, pp. 67646–67673, 2020.

[5] K. Ntontin and C. Verikoukis, "Relay-aided outdoor-to-indoor communication in millimeter-wave cellular networks," *IEEE Syst. J.*, vol. 14, no. 2, pp. 2473–2484, Jun. 2020.

[6] T. Bai and R. W. Heath, Jr., "Coverage and rate analysis for millimeter-wave cellular networks," *IEEE Trans. Wireless Commun.*, vol. 14, no. 2, pp. 1100–1114, Feb. 2015.

[7] T. S. Rappaport, R. W. Heath, Jr., R. C. Daniels, and J. N. Murdock, *Millimeter Wave Wireless Communications*. London, U.K.: Pearson, 2015.

[8] T. S. Rappaport, Y. Xing, O. Kanhere, S. Ju, A. Madanayake, S. Mandal, A. Alkhateeb, and G. C. Trichopoulos, "Wireless communications and applications above 100 GHz: Opportunities and challenges for 6G and beyond," *IEEE Access*, vol. 7, pp. 78729–78757, 2019.

[9] G. Yang and M. Xiao, "Performance analysis of millimeter-wave relaying: Impacts of beamforming and self-interference," *IEEE Trans. Commun.*, vol. 66, no. 2, pp. 589–600, Feb. 2018.

[10] K. Belbase, "Analysis of millimeter wave wireless relay networks," Ph.D. dissertation, Dept. Elect. Comput. Eng., Univ. Alberta, Edmonton, AB, Canada, 2019.

[11] M. Di Renzo, K. Ntontin, J. Song, F. H. Danufane, X. Qian, F. Lazarakis, J. De Rosny, D.-T. Phan-Huy, O. Simeone, R. Zhang, M. Debbah, G. Lerosey, M. Fink, S. Tretyakov, and S. Shamai (Shitz), "Reconfigurable intelligent surfaces vs. Relaying: Differences, similarities, and performance comparison," *IEEE Open J. Commun. Soc.*, vol. 1, pp. 798–807, 2020.

[12] E. Basar, M. Di Renzo, J. De Rosny, M. Debbah, M. Alouini, and R. Zhang, "Wireless communications through reconfigurable intelligent surfaces," *IEEE Access*, vol. 7, pp. 116753–116773, 2019.

[13] Q. Wu and R. Zhang, "Towards smart and reconfigurable environment: Intelligent reflecting surface aided wireless network," *IEEE Commun. Mag.*, vol. 58, no. 1, pp. 106–112, Jan. 2020.

[14] J. Park, S. Samarakoon, H. Shiri, M. K. Abdel-Aziz, T. Nishio, A. Elgabli, and M. Bennis, "Extreme URLLC: Vision, challenges, and key enablers," 2020, *arXiv:2001.09683*. [Online]. Available: http://arxiv.org/abs/2001.09683

[15] M. D. Renzo, A. Zappone, M. Debbah, M.-S. Alouini, C. Yuen, J. D. Rosny, and S. Tretyakov, "Smart radio environments empowered by reconfigurable intelligent surfaces: How it works, state of research, and road ahead," *IEEE J. Sel. Areas Commun.*, early access, Jul. 14, 2020, doi: 10.1109/JSAC.2020.3007211.

[16] M. Nemati, J. Ding, and J. Choi, "Short-range ambient backscatter communication using reconfigurable intelligent surfaces," in *Proc. IEEE Wireless Commun. Netw. Conf. (WCNC)*, May 2020, pp. 1–6.

[17] I. Trigui, W. Ajib, and W.-P. Zhu, "A comprehensive study of reconfigurable intelligent surfaces in generalized fading," 2020, *arXiv:2004.02922*. [Online]. Available: http://arxiv.org/abs/2004.02922

[18] S. B. Glybovski, S. A. Tretyakov, P. A. Belov, Y. S. Kivshar, and C. R. Simovski, "Metasurfaces: From microwaves to visible," *Phys. Rep.*, vol. 634, pp. 1–72, May 2016. [Online]. Available: http://www.sciencedirect.com/science/article/pii/S0370157316300618

[19] C. Liaskos, S. Nie, A. Tsioliaridou, A. Pitsillides, S. Ioannidis, and I. Akyildiz, "Realizing wireless communication through software-defined hyper surface environments," in *Proc. IEEE 19th Int. Symp. World Wireless, Mobile Multimedia Netw. (WoWMoM)*, Jun. 2018, pp. 14–15.

[20] G. Lavigne, K. Achouri, V. S. Asadchy, S. A. Tretyakov, and C. Caloz, "Susceptibility derivation and experimental demonstration of refracting metasurfaces without spurious diffraction," *IEEE Trans. Antennas Propag.*, vol. 66, no. 3, pp. 1321–1330, Mar. 2018.

[21] F. Liu, A. Pitilakis, M. S. Mirmoosa, O. Tsilipakos, X. Wang, A. C. Tasolamprou, S. Abadal, A. Cabellos-Aparicio, E. Alarcón, C. Liaskos, N. V. Kantartzis, M. Kafesaki, E. N. Economou, C. M. Soukoulis, and S. Tretyakov, "Programmable metasurfaces: State of the art and prospects," in *Proc. IEEE Int. Symp. Circuits Syst. (ISCAS)*, May 2018, pp. 1–5.

[22] L. Subrt and P. Pechac, "Controlling propagation environments using intelligent walls," in *Proc. 6th Eur. Conf. Antennas Propag. (EUCAP)*, Mar. 2012, pp. 1–5.

[23] C. You, B. Zheng, and R. Zhang, "Channel estimation and passive beamforming for intelligent reflecting surface: Discrete phase shift and progressive refinement," *IEEE J. Sel. Areas Commun.*, early access, Jul. 3, 2020, doi: 10.1109/JSAC.2020.3007056.

[24] M.-M. Zhao, Q. Wu, M.-J. Zhao, and R. Zhang, "Exploiting amplitude control in intelligent reflecting surface aided wireless communication with imperfect CSI," 2020, *arXiv:2005.07002*. [Online]. Available: http://arxiv.org/abs/2005.07002

[25] X. Guan, Q. Wu, and R. Zhang, "Anchor-assisted intelligent reflecting surface channel estimation for multiuser communications," 2020, *arXiv:2008.00622*. [Online]. Available: http://arxiv.org/abs/2008.00622

[26] Y. Han, S. Zhang, L. Duan, and R. Zhang, "Cooperative double-IRS aided communication: Beamforming design and power scaling," *IEEE Wireless Commun. Lett.*, vol. 9, no. 8, pp. 1206–1210, Aug. 2020.

[27] M.-M. Zhao, A. Liu, and R. Zhang, "Outage-constrained robust beamforming for intelligent reflecting surface aided wireless communication," 2020, *arXiv:2007.10769*. [Online]. Available: http://arxiv.org/abs/2007.10769

[28] J. G. Andrews, T. Bai, M. N. Kulkarni, A. Alkhateeb, A. K. Gupta, and R. W. Heath, Jr., "Modeling and analyzing millimeter wave cellular systems," *IEEE Trans. Commun.*, vol. 65, no. 1, pp. 403–430, Jan. 2017.

[29] S. Singh, F. Ziliotto, U. Madhow, E. Belding, and M. Rodwell, "Blockage and directivity in 60 GHz wireless personal area networks: From cross-layer model to multihop MAC design," *IEEE J. Sel. Areas Commun.*, vol. 27, no. 8, pp. 1400–1413, Sep. 2009.

[30] S. Biswas, S. Vuppala, J. Xue, and T. Ratnarajah, "On the performance of relay aided millimeter wave networks," *IEEE J. Sel. Topics Signal Process.*, vol. 10, no. 3, pp. 576–588, Apr. 2016.

[31] S. Gong, X. Lu, D. T. Hoang, D. Niyato, L. Shu, D. I. Kim, and Y.-C. Liang, "Towards smart wireless communications via intelligent reflecting surfaces: A contemporary survey," *IEEE Commun. Surveys Tuts.*, early access, Jun. 22, 2020, doi: 10.1109/COMST.2020.3004197.

[32] Y. Liu, X. Liu, X. Mu, T. Hou, J. Xu, Z. Qin, M. Di Renzo, and N. Al-Dhahir, "Reconfigurable intelligent surfaces: Principles and opportunities," 2020, *arXiv:2007.03435*. [Online]. Available: http://arxiv.org/abs/2007.03435

[33] Q. Wu, S. Zhang, B. Zheng, C. You, and R. Zhang, "Intelligent reflecting surface aided wireless communications: A tutorial," 2020, *arXiv:2007.02759*. [Online]. Available: http://arxiv.org/abs/2007.02759

[34] T. Hou, Y. Liu, Z. Song, X. Sun, Y. Chen, and L. Hanzo, "Reconfigurable intelligent surface aided NOMA networks," *IEEE J. Sel. Areas Commun.*, early access, Jul. 3, 2020, doi: 10.1109/JSAC.2020.3007039.

[35] X. Yue and Y. Liu, "Performance analysis of intelligent reflecting surface assisted NOMA networks," 2020, *arXiv:2002.09907*. [Online]. Available: http://arxiv.org/abs/2002.09907

[36] C. Zhang, W. Yi, Y. Liu, Z. Qin, and K. Keong Chai, "Downlink analysis for reconfigurable intelligent surfaces aided NOMA networks," 2020, *arXiv:2006.13260*. [Online]. Available: http://arxiv.org/abs/2006.13260

[37] C. Zhang, W. Yi, and Y. Liu, "Reconfigurable intelligent surfaces aided multi-cell NOMA networks: A stochastic geometry model," 2020, *arXiv:2008.08457*. [Online]. Available: http://arxiv.org/abs/2008.08457

[38] A.-A. A. Boulogeorgos and A. Alexiou, "Ergodic capacity analysis of reconfigurable intelligent surface assisted wireless systems," 2020, *arXiv:2008.01931*. [Online]. Available: http://arxiv.org/abs/2008.01931

[39] M. A. Kishk and M.-S. Alouini, "Exploiting randomly-located blockages for large-scale deployment of intelligent surfaces," *IEEE J. Sel. Areas Commun.*, early access, Aug. 24, 2020, doi: 10.1109/JSAC.2020.3018808.

[40] T. Hou, Y. Liu, Z. Song, X. Sun, Y. Chen, and L. Hanzo, "MIMO assisted networks relying on large intelligent surfaces: A stochastic geometry model," 2019, *arXiv:1910.00959*. [Online]. Available: http://arxiv.org/abs/1910.00959

[41] M. Di Renzo and J. Song, "Reflection probability in wireless networks with metasurface-coated environmental objects: An approach based on random spatial processes," *EURASIP J. Wireless Commun. Netw.*, vol. 2019, no. 1, p. 99, Dec. 2019.

[42] J. He, K. Yu, and Y. Shi, "Coordinated passive beamforming for distributed intelligent reflecting surfaces network," 2020, *arXiv:2002.05915*. [Online]. Available: http://arxiv.org/abs/2002.05915

[43] Q.-U.-A. Nadeem, A. Kammoun, A. Chaaban, M. Debbah, and M.-S. Alouini, "Asymptotic max-min SINR analysis of reconfigurable intelligent surface assisted MISO systems," *IEEE Trans. Wireless Commun.*, early access, Apr. 4, 2020, doi: 10.1109/TWC.2020.2986438.

[44] J. Lyu and R. Zhang, "Spatial throughput characterization for intelligent reflecting surface aided multiuser system," *IEEE Wireless Commun. Lett.*, vol. 9, no. 6, pp. 834–838, Jun. 2020.

[45] E. Basar and I. Yildirim, "SimRIS channel simulator for reconfigurable intelligent surfaces in future wireless networks," 2020, *arXiv:2008.01448*. [Online]. Available: http://arxiv.org/abs/2008.01448

[46] J. G. Andrews, F. Baccelli, and R. K. Ganti, "A tractable approach to coverage and rate in cellular networks," *IEEE Trans. Commun.*, vol. 59, no. 11, pp. 3122–3134, Nov. 2011.

[47] M. Rebato, J. Park, P. Popovski, E. De Carvalho, and M. Zorzi, "Stochastic geometric coverage analysis in mmWave cellular networks with realistic channel and antenna radiation models," *IEEE Trans. Commun.*, vol. 67, no. 5, pp. 3736–3752, May 2019.

[48] D. Moltchanov, "Distance distributions in random networks," *Ad Hoc Netw.*, vol. 10, no. 6, pp. 1146–1166, Aug. 2012. [Online]. Available: http://www.sciencedirect.com/science/article/pii/S1570870512000224

[49] Z. L. Fazliu, F. Malandrino, C. F. Chiasserini, and A. Nordio, "MmWave beam management in urban vehicular networks," *IEEE Syst. J.*, early access, Jun. 8, 2020, doi: 10.1109/JSYST.2020.2996909.

[50] J. Park, S.-L. Kim, and J. Zander, "Tractable resource management with uplink decoupled millimeter-wave overlay in ultra-dense cellular networks," *IEEE Trans. Wireless Commun.*, vol. 15, no. 6, pp. 4362–4379, Jun. 2016.

[51] Y. Li, J. G. Andrews, F. Baccelli, T. D. Novlan, and C. J. Zhang, "Design and analysis of initial access in millimeter wave cellular networks," *IEEE Trans. Wireless Commun.*, vol. 16, no. 10, pp. 6409–6425, Oct. 2017.

[52] J. Kim, J. Park, S. Kim, S. Kim, K. W. Sung, and K. S. Kim, "Millimeter-wave interference avoidance via building-aware associations," *IEEE Access*, vol. 6, pp. 10618–10634, 2018.

[53] A. K. Gupta, J. G. Andrews, and R. W. Heath, Jr., "On the feasibility of sharing spectrum licenses in mmWave cellular systems," *IEEE Trans. Commun.*, vol. 64, no. 9, pp. 3981–3995, Sep. 2016.

[54] K. Venugopal, M. C. Valenti, and R. W. Heath, Jr., "Interference in finite-sized highly dense millimeter wave networks," in *Proc. Inf. Theory Appl. Workshop (ITA)*, Feb. 2015, pp. 175–180.

[55] K. Belbase, Z. Zhang, H. Jiang, and C. Tellambura, "Coverage analysis of millimeter wave decode-and-forward networks with best relay selection," *IEEE Access*, vol. 6, pp. 22670–22683, 2018.

[56] M. Nemati, T. Baykas, and J. Choi, "Performance of TDOA and AOA localization techniques for different base-stations topologies," in *Proc. 13th Int. Conf. Signal Process. Commun. Syst. (ICSPCS)*, Dec. 2019, pp. 1–7.

[57] J. Lyu and R. Zhang, "Hybrid active/passive wireless network aided by intelligent reflecting surface: System modeling and performance analysis," 2020, *arXiv:2004.13318*. [Online]. Available: http://arxiv.org/abs/2004.13318

[58] V. Giurgiutiu, "Piezoelectric wafer active sensors," in *Structural Health Monitoring of Aerospace Composites*, V. Giurgiutiu, Ed. Oxford, U.K.: Academic, 2016, pp. 177–248, ch. 6. [Online]. Available: http://www.sciencedirect.com/science/article/pii/B9780124096059000064

[59] X. Zhang and M. Haenggi, "The performance of successive interference cancellation in random wireless networks," *IEEE Trans. Inf. Theory*, vol. 60, no. 10, pp. 6368–6388, Oct. 2014.

[60] M. Haenggi and R. K. Ganti, "Interference in large wireless networks," *Found. Trends Netw.*, vol. 3, no. 2, pp. 127–248, Jan. 2008.

[61] P. Frenger, J. Hederen, M. Hessler, and G. Interdonato, "Improved antenna arrangement for distributed massive MIMO," WO Patent 2 018 103 897, Jan. 26, 2017. [Online]. Available: https://patentscope.wipo.int/search/en/detail.jsf?docId=WO2018103897

[62] D. M. Pozar, S. D. Targonski, and H. D. Syrigos, "Design of millimeter wave microstrip reflectarrays," *IEEE Trans. Antennas Propag.*, vol. 45, no. 2, pp. 287–296, Feb. 1997.

[63] C. Huang, S. Hu, G. C. Alexandropoulos, A. Zappone, C. Yuen, R. Zhang, M. Di Renzo, and M. Debbah, "Holographic MIMO surfaces for 6G wireless networks: Opportunities, challenges, and trends," *IEEE Wireless Commun.*, early access, Jul. 8, 2020, doi: 10.1109/MWC.001.1900534.

JIHONG PARK (Member, IEEE) received the B.S. and Ph.D. degrees from Yonsei University, Seoul, South Korea, in 2009 and 2016, respectively. He was a Postdoctoral Researcher with Aalborg University, Denmark, from 2016 to 2017, and the University of Oulu, Finland, from 2018 to 2019. He is currently a Lecturer with the School of IT, Deakin University, Australia. His research interests include ultra-dense/ultra-reliable/mmWave system designs using stochastic geometry, as well as distributed learning/control/ledger technologies and their applications for beyond 5G/6G communication systems. He served as a Conference/Workshop Program Committee Member for the IEEE GLOBECOM, ICC, and WCNC, as well as for NeurIPS, ICML, and IJCAI. He received the IEEE GLOBECOM Student Travel Grant in 2014, the IEEE Seoul Section Student Paper Contest Bronze Prize in 2014, and the 6th IDIS-ETNEWS (The Electronic Times) Paper Contest Award sponsored by the Ministry of Science, ICT, and Future Planning of Korea. He is currently an Associate Editor of *Frontiers in Data Science for Communications*, a Review Editor of *Frontiers in Aerial and Space Networks*, and a Guest Editor of *Telecom* (MDPI).

JINHO CHOI (Senior Member, IEEE) was born in Seoul, South Korea. He received the B.E. degree *(magna cum laude)* in electronics engineering from Sogang University, Seoul, in 1989, and the M.S.E. and Ph.D. degrees in electrical engineering from the Korea Advanced Institute of Science and Technology (KAIST), in 1991 and 1994, respectively. He is currently a Professor with the School of Information Technology, Deakin University, Burwood, Australia. Prior to joining Deakin in 2018, he was with Swansea University, U.K., as a Professor/Chair in Wireless, and the Gwangju Institute of Science and Technology (GIST), South Korea, as a Professor. His research interests include the Internet of Things (IoT), wireless communications, and statistical signal processing. He authored two books published by Cambridge University Press, in 2006 and 2010. He received the 1999 Best Paper Award for Signal Processing from EURASIP and the 2009 Best Paper Award from WPMC (Conference). He is currently an Editor of the IEEE TRANSACTIONS ON COMMUNICATIONS and the IEEE WIRELESS COMMUNICATIONS LETTERS and a Division Editor of *Journal of Communications and Networks* (JCN). He had also served as an Associate Editor or Editor for other journals, including the IEEE COMMUNICATIONS LETTERS, JCN, the IEEE TRANSACTIONS ON VEHICULAR TECHNOLOGY, and *ETRI Journal*.

• • •

MAHYAR NEMATI (Member, IEEE) received the B.S. degree in electrical engineering and telecommunications from the University of Tehran, Iran, in 2015, and the M.S. degree in electrical, electronics, and cyber systems from Istanbul Medipol University, Turkey, in 2017. He is currently a Research Assistant with the School of IT, Deakin University, where he is involved in the field of wireless communications. His research interests in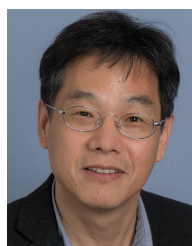clude digital communications, signal processing techniques at the physical and medium access layer, multi-carrier schemes, waveform design in wireless networks, the IoT, MTC, and URLLC.